JOURNAL OF THERMOPHYSICS AND HEAT TRANSFER
Vol. 19, No. 2, April–June 2005

Convection and Solidification in Constant and Oscillating Thermal Gradients: Measurements and Simulations

Y. Shu* and B. Q. Li†
Washington State University, Pullman, Washington 99163
and
H. C. de Groh, III‡
NASA John H. Glenn Research Center at Lewis Field, Cleveland, Ohio 44135

An experimental and numerical study of natural convection and solidification in a two-dimensional cavity driven by constant and oscillating temperature gradients is presented. Finite element models are developed to predict the flowfield, the temperature distribution, and the solid–liquid interphase shapes during solidification. Both the fixed-grid and moving-grid methods are applied in the numerical simulations, using the former to illustrate the oscillating thermal gradient conditions and using the latter to illustrate the constant temperature gradient conditions. An experimental system is set up where succinonitrile is used as a working fluid. The flow pattern, the velocity field, and the solidification interface shape are measured using the laser-based particle-image-velocimetry system. Numerical simulations and experiments are conducted for various configurations and different thermal gradients. In most cases, convection is dominated by one recirculating loop. With an inverted temperature gradient, however, multiple convection loops are observed. Both the convective flow pattern and the velocity strongly affect the solid–liquid interface shapes during solidification. In a majority of the cases studied, the model predictions are in good agreement with the experimental measurements.

Nomenclature

C_p	=	specific heat
f	=	frequency of temperature modulation
$\boldsymbol{g}_0$	=	terrestrial gravity
H	=	height of the cavity
$\hat{\boldsymbol{i}}, \hat{\boldsymbol{j}}$	=	unit vectors in the x and y directions, respectively
k	=	thermal conductivity
L	=	length of the cavity
Pr	=	Prandtl number
p	=	pressure
$\boldsymbol{q}_T$	=	boundary heat flux
Ra	=	Rayleigh number
S	=	interface
St_e	=	Stefan number
T	=	temperature
T_m	=	melting point
t	=	time
$U_{\max}$	=	absolute value of maximum velocity
$\boldsymbol{u}$	=	velocity
α	=	thermal diffusivity
β	=	thermal expansion coefficient
ΔH	=	latent heat
ΔT	=	temperature difference between two sidewalls
ε_p	=	penalty parameter for pressure
θ	=	shape function for temperature
μ	=	dynamic viscosity
ν	=	kinematic viscosity
ρ	=	density
τ	=	stress tensor
ϕ	=	shape function for velocity
ψ	=	shape function for pressure
Ω, $\partial\Omega$	=	computational domain and boundary of the domain

Subscripts

B, T, L, R	=	bottom, top, left, and right sidewalls
l	=	liquid
n	=	normal direction
s	=	solid
t	=	tangential direction

Received 5 March 2004; revision received 29 June 2004; accepted for publication 2 July 2004.

*Research Associate, School of Mechanical and Materials Engineering.
†Professor, School of Mechanical and Materials Engineering; li@mme.wsu.edu.
‡Senior Scientist.

I. Introduction

SOLIDIFICATION is a basic phenomenon in melt processing systems for metals and other materials. During solidification, the existence of thermal gradients causes natural convection in the liquid. This convection is thought to be responsible for structural defects and inhomogeneity in the final products. Because of its engineering significance, the effect of fluid flow on solidification has been studied extensively by the research community. Literature in this area ranges from that which provides a fundamental understanding of the solidification process to that which explains the process's practical applications.[1–4] The new applications of solidification processing and also the need to improve our understanding of the basics governing the liquid–solid transitions have been the major thrust for the continuous emergence of research work on this subject.[5–9]

Because most liquid metals and semiconductor melts are opaque, fundamental studies on the effect of convection on solidification are conducted on transparent fluids to permit flow visualization. Succinonitrile (SCN), which has some properties similar to liquid metals, has recently become a fluid of choice for solidification studies. Yeoh et al.[10] and Simpson et al.[11] reported their numerical and experimental studies on solidification of SCN in a horizontal Bridgman apparatus. Their measurements largely focused on the interface shapes in steady-state conditions. Results showed that the solid–liquid interface was significantly distorted into a complex-curved shape by the natural convection in the liquid adjacent to the interface. Benielli et al.[12] investigated the correlation between the thermal convection and the pulling rate on the interface morphological

instability of a SCN-acetone alloy and concluded that the interaction between thermal convection and pulling velocity results in different temperature distribution in the melt and hence various solid–liquid interface shapes. In those reports, only constant thermal gradients were considered, and the experimental visualization of the interaction between flow and the interface morphology was not presented.

Studies on solidification of other types of fluid have also been reported. Cao and Poulikakos[13,14] presented experimental results on the solidification of a NH_4Cl-water mixture in a rectangular cavity. They pointed out that the orientation of the imposed temperature gradients has a significant effect on the flow strength and interface shape. When cooled from the top, the flow was weak, and the interface was essentially flat, but the convective flow was strong and affected the interface shapes if an inclined temperature gradient was applied. Because only a qualitative comparison was available between the temperature distribution from measurements and from a theoretical model, the flow effect on interface was hard to tell from the images. Giangi et al.[15] investigated numerically and experimentally the natural convection during ice formation. Various boundary conditions were applied at the sidewalls such as fixed temperatures, adiabatic conditions, or constant heat flux. The enthalpy method was used to trace the interface. Results showed that a small variation of the heat flux or temperature could lead to a significant variation in the flowfield. Still, though, the information from experiments is very limited.

Convective flow patterns during solidification were studied by Davis et al.[16] in a pure material system. Rolls, hexagonal, or mixed patterns were observed in their experiments. Their measurements were focused on the instability criterion for various flow patterns in a horizontal layer with vertical temperature gradients, whereas solidification in a constraint cavity with edge effect and the flow contribution to the solid–liquid interface was not considered.

The effect of temperature oscillation on the interface shape during a vertical Bridgman growth process was recently investigated by Stelian et al.[17] The relationship between the interface velocity and the temperature modulation applied on the horizontal boundaries of a two-dimensional cavity was predicted numerically. They concluded that the interface oscillation follows the sinusoidal signals applied on top of the cavity with the same period, but with a phase difference. A discussion of how the oscillating temperature affects the interface shape, however, was not fully developed. Moreover, their numerical predictions need to be validated experimentally.

In addition to the effect of thermal gradients on convection and solidification, the body of research also examines the influences of initial concentrations or boundary conditions on the fluids. Pradeep et al.[18] investigated the boundary condition effects on solidification with a binary solution (ammonium chloride and water) in rectangular cavities. One cavity has three walls (two sidewall and one bottom wall) cooled, and the other cavity has only vertical walls cooled. They showed that vortex flow appeared at the corner of the chamber when cooled from bottom. Skudarnov et al.[19] carried out experiments to assess the effect of initial solute concentration on convection during solidification using the same solution as Ref. 18. Different flow patterns were detected in a melt with different initial concentrations.

As just discussed, experimental data on the transient convection and flow patterns as well as their effects on solidification are very limited, especially for pure materials or materials with a narrow melting temperature range. There is also a lack of understanding of the effect of oscillating temperature gradients on solidification, except for the numerical simulations by Stelian et al.[17]

This paper presents an experimental and numerical study of natural convection in solidifying liquids and describes the effect of natural convection on the solid–liquid interface morphology that developed under various imposed constant and oscillating thermal gradients. The intent is to understand better the fluid flow's effect on solidification and to quantify this effect through both numerical modeling and laboratory measurement. The numerical model is developed based on the deforming finite element solution of the Navier–Stokes equations for fluid flow and the energy transport equation for temperature distribution, with the solid–liquid interface morphology tracked by an arbitrary Eulerian–Lagrangian formulation. A laboratory solidification system consisting of a rectangular cavity is set up, and pure SCN (>99%) is used as the working fluid. In this system, the flow is driven by either constant or oscillating temperature fields. The solidification is induced by cooling one or more wall below the freezing point. The instantaneous velocity fields and flow patterns and the solidification front advancement and morphology were measured by a laser-based particle-image-velocimetry (PIV) system. Transient and steady no-growth conditions under fixed temperature gradients, as well as the periodic natural convection and solidification driven by sinusoidally oscillating wall temperatures, were studied experimentally and numerically. The convective flow patterns in the liquid pool as well as solid–liquid interface shapes measured experimentally are compared with those predicted by the finite element model.

II. Problem Statement

Figure 1 illustrates the two solidification systems to be studied. Figure 1a shows the study of solidification in constant temperature gradients, whereas Fig. 1b shows oscillating temperature fields. The width and the height of the cavity are L and H, respectively. Shown also in the systems are the direction of gravity and the coordinate system for analysis. Initially, both systems are filled with liquids at a fixed temperature.

In Fig. 1a, the top and bottom walls are adiabatic. The two sidewalls are kept at constant temperatures, with the right sidewall T_R maintained lower than the melting point T_m and the left sidewall T_L higher. Because of the existence of the thermal gradient in the system, natural convection arises in the liquid pool and is sketched qualitatively as shown in the figure. The convective flow is known to affect the temperature distribution in the system. Solidification starts from the right sidewall and advances towards the left until it reaches a steady, no-growth state. In the absence of fluid flow, the solidification front would be flat and parallel to the vertical walls.

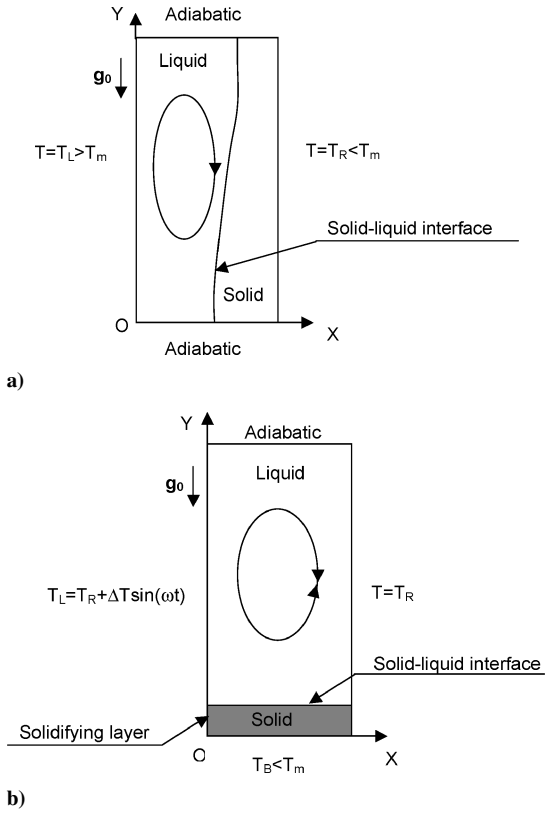

Fig. 1 Schematic diagram of solidification of SCN in a) constant and b) oscillating temperature fields.

When the convection is present, however, the solid–liquid interface is no longer vertical.

In Fig. 1b, the top wall is still kept adiabatic, but the bottom wall is kept at a constant temperature T_B lower than the melting point while the left sidewall $T_L(t)$ is equal to $T_R + \Delta T \sin(2\pi f t)$. This arrangement is used to study the solidification behavior under an oscillating temperature gradient. The modulated thermal gradient in the liquid pool interacts with the gravity to drive an oscillating convective flowfield, which affects both the temperature distribution and the solidification interface advancement and morphology. We note that in practice very few solidification processing systems under terrestrial conditions have been designed to operate with a modulated thermal gradient. However, the study of oscillating convection and its effect on solidification is important to the researchers who are concerned about the space processing systems that are influenced by gravity perturbation and to those researchers who design the vibration control mechanisms of solidification processing systems. In Fig. 1b, solidification commences at the bottom wall and advances upward toward the top.

The preceding two systems are studied using both numerical modeling and experimental measurements, which are described next.

III. Mathematical Formulation

The mathematical description of the melt's convection and heat transfer in the liquid pool is made by the continuity equation, the Navier–Stokes equations, and energy-balance equation, namely,

$$\nabla \cdot \boldsymbol{u} = 0 \tag{1}$$

$$\rho_l \left(\frac{\partial \boldsymbol{u}}{\partial t} + \boldsymbol{u} \cdot \nabla \boldsymbol{u} \right) = -\nabla p + \mu \nabla^2 \boldsymbol{u} - \rho_l \beta \boldsymbol{g}_0 [T_L(t) - T_m] \tag{2}$$

$$\rho_l C_{p,l} \left(\frac{\partial T_l}{\partial t} + \boldsymbol{u} \cdot \nabla T_l \right) = k_l \nabla^2 T_l \tag{3}$$

In the solid, there is no flow. Thus, the transport equation reduces to a heat-conduction equation,

$$\rho_s C_{p,s} \frac{\partial T_s}{\partial t} = k_s \nabla^2 T_s \tag{4}$$

The shape of the solidification front is determined by the thermal balance along the interface,

$$k_s (\hat{\boldsymbol{n}} \cdot \nabla T_s) - k_l (\hat{\boldsymbol{n}} \cdot \nabla T_l) = \rho \Delta H \frac{\mathrm{d}S}{\mathrm{d}t} \tag{5}$$

with the conditions that

$$T_s(S,t) = T_l(S,t) = T_m, \qquad \boldsymbol{u}_t = 0, \qquad \boldsymbol{u}_n = 0$$

To solve the preceding equations, appropriate boundary conditions need to be applied. For the system with constant temperature gradients, the following constraints are applied at the boundaries:

$$\boldsymbol{u} = 0 \qquad \text{at all boundaries}$$

$$T = T_L \qquad \text{at} \qquad x = 0$$

$$T = T_R \qquad \text{at} \qquad x = L$$

$$\frac{\partial T}{\partial y} = 0 \qquad \text{at} \qquad y = 0 \qquad \text{and} \qquad y = H$$

For the system with an oscillating temperature field, the nonslip boundary condition is still valid, while the thermal boundary conditions are as follows:

$$T = T_R + \Delta T \sin(2\pi f t) \qquad \text{at} \qquad x = 0$$

$$T = T_R \qquad \text{at} \qquad x = L$$

$$T = T_B \qquad \text{at} \qquad y = 0$$

$$\frac{\partial T}{\partial y} = 0 \qquad \text{at} \qquad y = H$$

IV. Numerical Solution

The governing equations just described for the fluid flow and heat conduction/convection, along with the boundary conditions, are solved using the deforming Galerkin finite element method. Following the procedures in previous studies, the governing equations are recast in the integral forms[20]:

$$\left(\int_\Omega \psi \hat{\boldsymbol{i}} \cdot \nabla \phi^T \, \mathrm{d}V \right) \boldsymbol{U}_i = -\varepsilon_p \left(\int_\Omega \psi \psi^T \, \mathrm{d}V \right) \boldsymbol{P} \tag{6}$$

$$\begin{aligned} &\left(\int_\Omega \rho \phi \phi^T \, \mathrm{d}V \right) \frac{\mathrm{d}\boldsymbol{U}_i}{\mathrm{d}t} + \left(\int_\Omega \rho \phi \boldsymbol{u} \cdot \nabla \phi^T \, \mathrm{d}V \right) \boldsymbol{U}_i \\ &\quad - \left(\int_\Omega \hat{\boldsymbol{i}} \cdot \nabla \phi \psi^T \, \mathrm{d}V \right) \boldsymbol{P} + \left(\int_\Omega \mu \nabla \phi \cdot \nabla \phi^T \, \mathrm{d}V \right) \boldsymbol{U}_i \\ &\quad + \left[\int_\Omega \mu (\hat{\boldsymbol{i}} \cdot \nabla \phi)(\hat{\boldsymbol{j}} \cdot \nabla \phi^T) \, \mathrm{d}V \right] \boldsymbol{U}_j + \left(\int_\Omega \rho \beta \boldsymbol{g}_0 \phi \theta^T \, \mathrm{d}V \right) \boldsymbol{T} \\ &\quad = \int_{\partial\Omega} \boldsymbol{n} \cdot \tau \cdot \hat{\boldsymbol{i}} \phi \, \mathrm{d}S + \int_\Omega \rho \boldsymbol{g}_0 \beta \phi T_m \, \mathrm{d}V \end{aligned} \tag{7}$$

$$\begin{aligned} &\left(\int_\Omega \rho C_p \theta \theta^T \, \mathrm{d}V \right) \frac{\mathrm{d}\boldsymbol{T}}{\mathrm{d}t} + \left(\int_\Omega \rho C_p \theta \boldsymbol{u} \cdot \nabla \theta^T \, \mathrm{d}V \right) \boldsymbol{T} \\ &\quad + \left(\int_\Omega k \nabla \theta \cdot \nabla \theta^T \, \mathrm{d}V \right) \boldsymbol{T} = - \int_{\partial\Omega} \boldsymbol{q}_T \theta \, \mathrm{d}S \end{aligned} \tag{8}$$

Once the forms of shape functions ϕ, ψ, and θ for velocity, pressure, and all remaining scalars are specified, the integrals defined in the preceding equations can be expressed in the following element stiffness matrix equation:

$$\begin{bmatrix} \boldsymbol{M} & 0 \\ 0 & \boldsymbol{N} \end{bmatrix} \begin{bmatrix} \dot{\boldsymbol{U}} \\ \dot{\boldsymbol{T}} \end{bmatrix} + \begin{bmatrix} \boldsymbol{A}(\boldsymbol{U}) + \boldsymbol{K} + 1/\varepsilon_p \boldsymbol{E} \boldsymbol{M}_p^{-1} \boldsymbol{E}^T & \boldsymbol{B} \\ 0 & \boldsymbol{D}(\boldsymbol{U}) + \boldsymbol{L} \end{bmatrix} \begin{bmatrix} \boldsymbol{U} \\ \boldsymbol{T} \end{bmatrix} = \begin{bmatrix} \boldsymbol{F} \\ \boldsymbol{G} \end{bmatrix} \tag{9}$$

Note that in constructing the preceding element matrix equation, the penalty formulation has been applied, and $\boldsymbol{P}$ in the momentum equation is replaced by $(1/\varepsilon_p)\boldsymbol{M}_p^{-1}\boldsymbol{E}^T\boldsymbol{U}$. The assembled global matrix equations are stored in the skyline form and solved using the Gaussian elimination method. The coefficient matrices of Eq. (9) are calculated by

$$\boldsymbol{M}_p = \int_\Omega \psi \psi^T \, \mathrm{d}V \qquad \boldsymbol{N} = \int_\Omega \rho C_p \theta \theta^T \, \mathrm{d}V$$

$$\boldsymbol{M} = \int_\Omega \rho \phi \phi^T \, \mathrm{d}V \qquad \boldsymbol{A}(\boldsymbol{U}) = \int_\Omega \rho \phi \boldsymbol{u} \cdot \nabla \phi^T \, \mathrm{d}V$$

$$\boldsymbol{E}_i = \int_\Omega \hat{\boldsymbol{i}} \cdot \nabla \phi \psi^T \, \mathrm{d}V \qquad \boldsymbol{D}(\boldsymbol{U}) = \int_\Omega \rho C_p \theta \boldsymbol{u} \cdot \nabla \theta^T \, \mathrm{d}V$$

$$\boldsymbol{L} = \int_\Omega k \nabla \theta \cdot \nabla \theta^T \, \mathrm{d}V \qquad \boldsymbol{B} = \int_\Omega \left(\rho \boldsymbol{g}_0 \beta \phi \theta^T \right) \mathrm{d}V$$

$$\boldsymbol{G}_T = - \int_{\partial\Omega} \boldsymbol{q}_T \theta \, \mathrm{d}S \qquad \boldsymbol{F} = \int_{\partial\Omega} \boldsymbol{n} \cdot \tau \phi \, \mathrm{d}S + \int_\Omega \rho \boldsymbol{g}_0 \beta \phi T_m \, \mathrm{d}V$$

$$\boldsymbol{K}_{ij} = \left(\int_\Omega \mu \nabla \phi \cdot \nabla \phi^T \, \mathrm{d}V \right) \delta_{ii} + \int_\Omega \mu (\hat{\boldsymbol{i}} \cdot \nabla \phi)(\hat{\boldsymbol{j}} \cdot \nabla \phi^T) \, \mathrm{d}V$$

Although various techniques can be applied to treat the moving boundary term [Eq. (5)], this study applies an iterative procedure. An arbitrary Eularian–Lagrangian deforming finite element approach is used to accurately track the solidification interface.[21] By this algorithm, the finite elements that cover the solidifying liquid and solid are deformed and the nodes within the region are allowed to move in accordance with the interface's movement. These additional velocities resulting from the mesh movement are added to the velocity field. Two basic algorithms can then be applied: one treats the moving interface as a separate variable and incorporates the interface thermal boundary condition into the global finite element matrix, and the other algorithm considers the interface thermal boundary condition as a separate constraint and solves it separately from the coupled field equations. Our numerical experience shows that in a majority of cases the incorporation of the isothermal constraint into the global matrix results in a very unstable nonlinear system. In fact, the whole system is extremely sensitive to boundary perturbations, and, more often than not, the perturbation leads to divergence. Separation of the moving interface boundary coordinates from the global finite element field variable solutions, on the other hand, requires the convergence of both moving interface coordinates and field variables in two related loops. In this case, the global finite element matrix has a smaller bandwidth and thus needs a shorter CPU time for the iteration of the field variables, which takes the majority of the computing time. Our tests further show that the two methods require approximately the same amount of CPU time, with the latter being much more robust and numerically stable. Therefore, the latter method has been employed in the present study.

In the case of oscillating thermal gradients, the solidification interface is highly distorted, making it difficult to apply the deforming finite elements as just discussed. Thus, the fixed-grid method, that is, the enthalpy method, is used instead,[15,22] subject to the caveats of the method for modeling the solidification of pure materials.

The computational procedure can now be summarized as follows: First, the temperature and velocity fields are solved using an initial guess of the solid–liquid interface and with the latent heat treated as a prescribed surface source along the interface. The solid–liquid interface position, which is marked by a constant melting temperature, is then interpolated based on the temperature distribution. The updated interface is used to recalculate the temperature and flowfields. The calculation repeats for each time step until the unknowns (temperature, velocity, and interface position) are simultaneously within a preset tolerance. An implicit time scheme with automatic time stepping is used to carry out the time matching.

V. Experimental Setup and Procedures

A. Experimental System Setup

The experimental system for flow and interface position measurements is schematically sketched in Fig. 2. The whole system consists of three computers, a laser, a charge-coupled-device (CCD) camera, a test cell, a heater strip, three isothermal water baths, and some accessories. The main part of the system is a rectangular cavity of $6.2 \times 20 \times 120$ mm^3. The two sidewalls of the cavity are made of 3.16-mm-thick copper in order to ensure good heat conduction. The other walls are made of 6.35-mm-thick fused silica for flow visualization. The top and bottom planes are covered with insulating foam, and a slit of 1 mm width is cut through the foam, 1 in. (25.4 mm) away from the front plate of the cavity, so that the laser sheet can illuminate the vertical plane for visualization. To prevent the copper sidewalls from reflecting laser light, the inside surfaces are painted

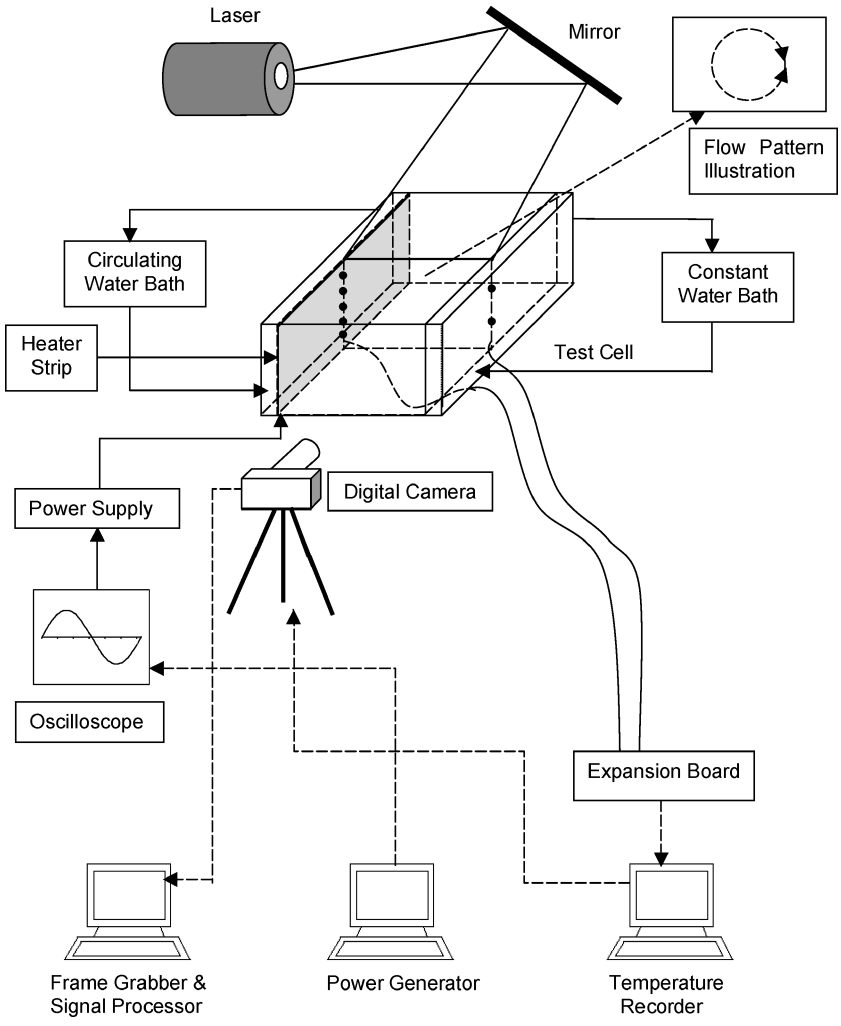

Fig. 2 Schematic diagram of the laser-based PIV experimental system setup.

matte black. There is a heater strip glued to the outer side of the left copper wall for the purpose of temperature oscillation. The working material is SCN, which it is transparent in its liquid phase.

The function of the computer on the right is to collect temperature data and to control the shutter of the CCD camera for flow visualization and PIV measurements. The middle computer controls the heater strip mounted on the test cell. It uses its own counter board and sends signals to the ac power amplifier to generate the oscillating electrical wave required to produce an oscillating temperature field. The computer on the left is a dual-processor PC, designed to perform data-intensive computations for image processing. It combines image capturing and image processing into one unit. This computer is synchronized with the computer on the right to obtain temperature and velocity data simultaneously.

The PIV system used in this experiment consists of three parts: visualization equipment (laser), image recording equipment (CCD camera), and analysis software (Insight NT). The ion laser (Stabilite 2017) is from Spectra Physics Laser, Inc., and argon is used as an excitation medium. The Model 630044D PIVCAM 4-30 CCD video camera from TSI offers 748×486 pixels resolution and has a frame rate as fast as 30 frames per second. Compared with the slow flow motion in the current experiments, this camera is fast and accurate enough for time-sequenced measurements. The camera also has a terminal allowing Insight-NT software or external signals to control it. The postprocessing software, Insight-NT, is used to analyze the images. Additionally, this software provides a platform for Tecplot for further interpretation. In the present cases, two-frame cross correlation is used for image processing. The estimated uncertainty in the velocity measurements is ±0.04 mm/s. The resolution of each x and y component of the velocity is 0.3×0.50 mm in space and 200 ms in time.

The seeding particles used in these experiments are silica sphere with a nominal diameter of 70 μm and a specific gravity of 1.01. The concentration of the particles is nearly 8.7×10^{-4} g/ml. The selection of the particles is based on the criteria stated in Ref. 23.

B. Experimental Procedures

Because SCN is solid at room temperature ($T_m = 331.23$ K), a temperature 1 K higher than the melting point is applied to both sides of the cavity to melt the SCN. The estimated uncertainty with temperature measurements is $\pm0.01^\circ$C. After melting, the temperatures of the thermal baths are adjusted to the desired temperature on both sidewalls. For solidification experiments in constant temperature gradients, the left sidewall is kept at a temperature higher than T_m, while the right sidewall is kept at a fixed temperature lower than T_m. Solidification gradually starts from the right sidewall and reaches a steady, zero-growth state after a sufficiently long time. To obtain the oscillating temperature gradients (model in Fig. 1b), a third water circulator is connected to the bottom plate of the cavity to provide a constant temperature T_B lower than T_m. The heater on the left sidewall is turned on, and the temperature of the left wall oscillates sinusoidally with its mean temperature approximately equal to the right wall temperature.

VI. Results and Discussions

The preceding numerical model and experimental system have been used to study the fluid flow, temperature distribution, and interface morphology for various conditions. The numerically obtained results are compared with the experimental measurements. The mesh sensitivity test was performed for the enthalpy method prior to the numerical simulation. The condition applied for the test is the same as in Fig. 1a, which has a constant temperature gradient. Tests showed that 21×41 grids with a uniform mesh distribution gave an optimal choice for the computation. To start the solidification calculation using the front tracking method, an initially assumed solid layer must exist. Hence, a cold wall covered with solid SCN of 0.01 mm thick was applied prior to the calculation. The solid and liquid regions are each discretized using a uniform mesh of 11×41 grids. The results obtained using the enthalpy and moving-grid methods agree within the machine accuracy for the same given conditions.

Table 1 Physical properties of pure succinonitrile

Description	Symbol	Value
Thermal conductivity of liquid, W/m · K	k_l	0.223
Thermal conductivity of solid, W/m · K	k_s	0.225
Density of liquid, kg/m^3	ρ_l	990
Density of solid, kg/m^3	ρ_s	990
Specific heat of liquid, J/kg · K	$C_{p,l}$	2000
Specific heat of solid, J/kg · K	$C_{p,s}$	1955
Thermal expansion coefficient, 1/K	β_T	-8.1×10^{-4}
Dynamic viscosity, N · s/m^2	μ	3.0×10^{-3}
Melting temperature, $^\circ$C	T_m	58.08
Latent heat, J/kg	ΔH	4.624×10^4

The thermophysical properties of SCN used for calculations are given in Table 1 (see also Ref. 10). Detailed scaling analysis for this problem is provided in Ref. 24. With the measured temperature and the characteristic length 6.2 mm (dimension of the cavity in x direction), the nondimensional parameters for the system being studied are the Rayleigh number $Ra \sim 10^4$, Prandtl number $Pr = 27$, and Stefan number $St_e = 0.2$, where $Ra = g\beta\Delta T L^3/\nu\alpha$, $Pr = \nu/\alpha$, and $St_e = C_p\Delta T/\Delta H$.

A. Constant Temperature Gradients

Figure 3 depicts a set of snapshots of calculated and measured velocity and solidification front morphology that are evolving with time to a quasi steady state. Clearly, numerical predictions obtained from the finite element model compare well with the PIV measurements within the major part of the domain. The imperfections of the PIV pictures near the bottom and the top are thought to be caused by the laser light condition. Because the front plate of the cavity cannot be thermally insulated because of the camera's position, solidification can sometimes occur at the front top and bottom corner of the cavity. Thus, the real situation at the cross section the laser beam goes through might be hidden by a small layer of solid SCN near the bottom and the top of the front plate. Therefore, meaningful comparisons cannot be made at the regions very close to the top and the bottom. Numerical simulations further confirmed that the heat loss from the slit cut on the foam produces no noticeable change in predicted results for all of the cases, except those with an inverse thermal gradient (see Sec. VI.C). In addition, the solidification front morphology can be various, depending on the position of the interface being measured[11] and the freezing time.[15]

For all of the figures presented in this paper, I indicates the experimental images, II the calculated velocity profile using measured temperature data, and III the comparison of interface between experimental measurement (dot) and numerical prediction (solid line), unless elsewhere mentioned. Examination of these results further shows that solidification commences from the right wall where the temperature is set below the melting point. Initially (for up to 2 min), the solid–liquid interface is essentially flat with a little tilt along the vertical walls (see Fig. 3a). This suggests that during the initial stage the solidification interface shape is mainly controlled by the heat conduction through a thin layer solidified near the cold wall. The convection in the liquid pool assumes approximately a rectangular loop with the cold fluid washing down along the solid–liquid interface and hot fluid rising upwards along the left wall, displaying the nature of free convection driven by the thermally induced buoyancy forces. The effect of convection is minimal on the solid–liquid interface shape, which is evident by both experimental measurements and numerical predictions.

As solidification progresses, the interaction between convection and solidification in the solidifying liquid becomes more pronounced. This is clearly illustrated by the ensuing figures in the sequence. Comparison of these results reveals that while the convection cell remains as one single recirculating loop the maximum velocity becomes progressively smaller. The solidification interface shape evolves differently from the initial stage, however. Near the top right corner, the solidification process almost ceases to continue after the initial stage. This is attributed to the fact that the fluid obtains the highest thermal energy after climbing upward along the hot

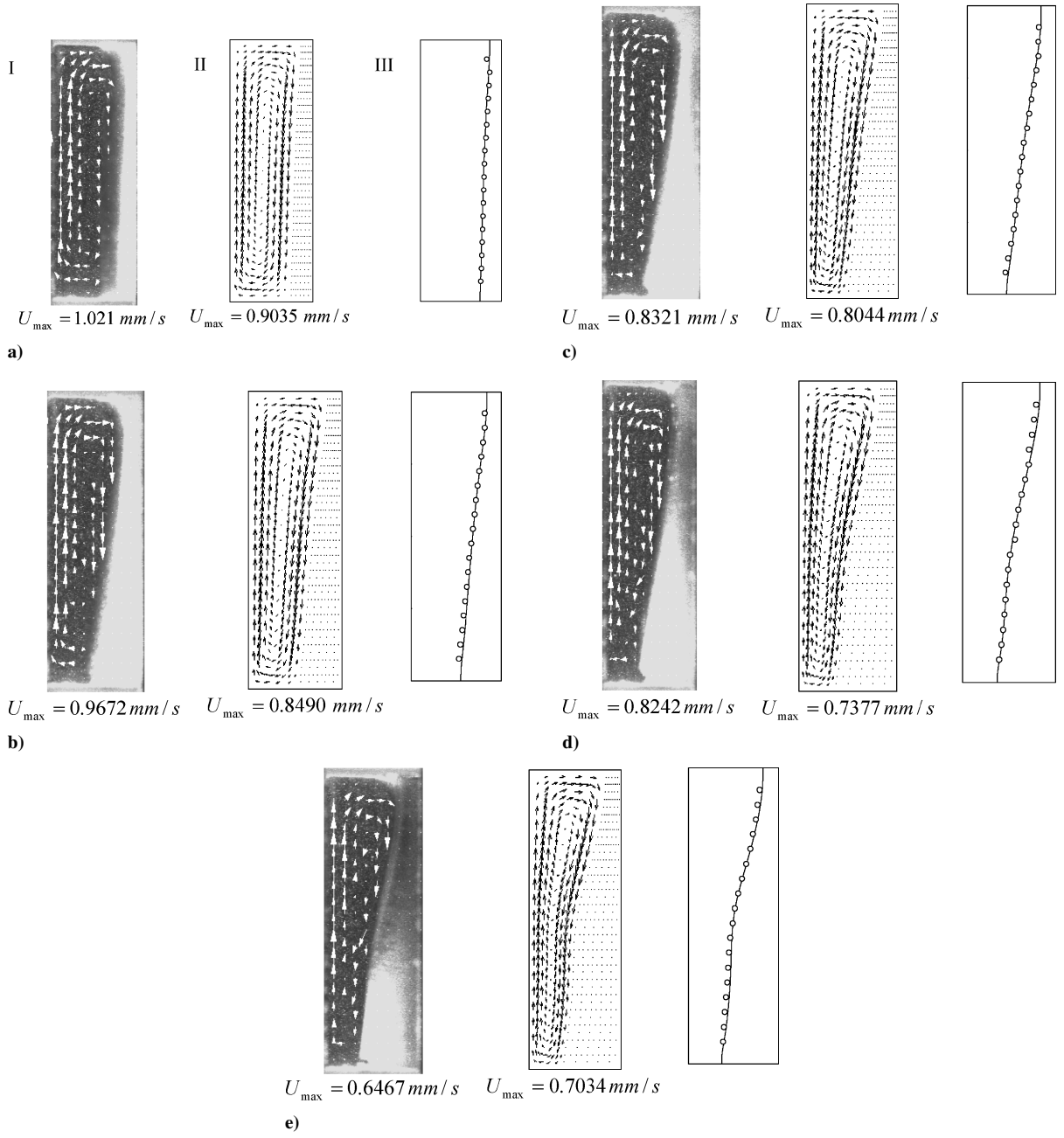

Fig. 3 Evolution of velocity and solid–liquid interface during solidification (T_L = 334.12 K, T_R = 328.61 K). Plot region: 6.2 × 20 mm (cross section): a) t = 2 min, b) t = 6 min, c) t = 10 min, d) t = 20 min, and e) t = 40 min.

wall but is forced by mass conservation to be in contact with the cold solidification front. As the hot fluid is dragged down along the solid–liquid interface by gravity, it loses its thermal energy to the solid and starts to solidify. The heat lost by the fluid and also the latent heat released as a result of solidification are conducted through the solid layer on the cold wall and are eventually carried away by the SCN circulating through the thermal bath. The fluid becomes coolest when it reaches the bottom and then is forced by convection to go upwards along the hot wall. Consequently, the solid layer is thickest at the bottom. This basic physical picture is well predicted by the finite element model and is verified by the experimental measurements. Further details of the solidification interface shape evolution resulting from the convection effects show a distorted solid–liquid front morphology in both computed and measured results (see Figs. 3d and 3e). From the time $t = 2$ min to the final quasi steady state, the strength of the convective flow decreases only about 22%, but the interface is moved by more than 200%, measured from the plane of $y = 0$. The discrepancy for the maximum velocity is less than 12% between measurement and simulation and within 3% for the interface location.

Both numerical predictions and experimental measurements show that the transient development of solid–liquid morphology and convection is very similar to that discussed above for other solidification experiments. Thus, for the sake of brevity, only the steady-state results are presented for these cases.

Figure 4 shows the velocity fields, convection patterns, and solidification interface shapes for three different thermal gradients. Once again, for all of these cases numerical predictions are in excellent agreement with the experimental measurements. For these cases, the temperature of the right sidewall was kept at 328.65 K, whereas the temperature of the left sidewall is adjusted between 336.15 ~ 333.65 K. The measured wall temperatures from the experiments were input into the mathematical model (shown in Fig. 1a) to obtain numerical results for comparison. Both computed results and experimental measurements show that for all of these cases a single recirculating loop is developed in the liquid pool, which is

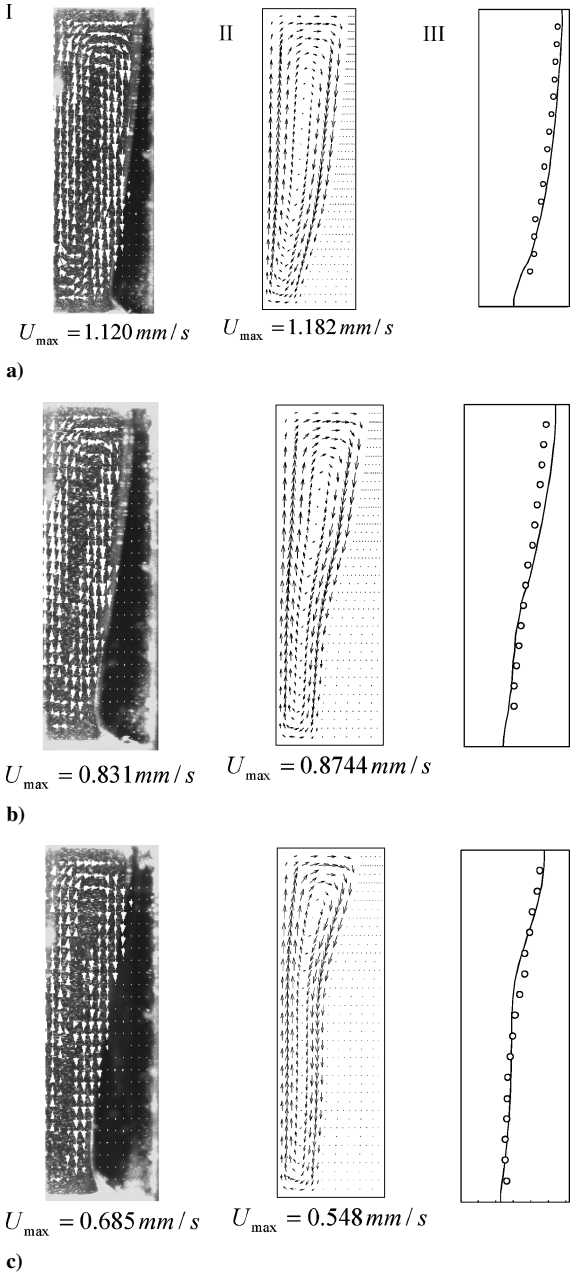

Fig. 4 Solidification of SCN under fixed temperature gradients in a vertical cell. Plot region: 6.2 × 20 mm: a) $T_L = 336.15$ K, $T_R = 328.65$ K; b) $T_L = 334.65$ K, $T_L = 328.65$ K; and c) $T_L = 333.65$ K, $T_R = 328.65$ K.

attributed to the buoyancy force. However, the strength of the flow weakens with the decrease of temperature gradients between sidewalls. Comparison of these figures also indicates that the velocity does not respond linearly to the change in thermal gradients. When the temperature gradient decreased about 30%, the maximum velocity drops by about 50% (see Figs. 4a and 3c). This demonstrates the nonlinear interaction between velocity and temperature difference in distributing momentum in the liquid pool.

The strong convection induced in the liquid pool exerts a profound influence on the interface shape, as is evident in Fig. 4. In the absence of convection, the solid–liquid interface would be flat, which, as a check, is confirmed by additional numerical simulations using both fixed and moving grids. In the presence of convection, the interface exhibits a nonflat shape such that a thin solid layer exists at the top-right corner and the solid layer gradually increases in thickness down along the right wall, which is caused by convection as already described. By decreasing the temperature of the left sidewall without changing that of the right wall, the interface moves toward the left, as expected. It is seen that convection is less vigorous with a smaller temperature gradient and produces a less distorted solid–liquid interface shape, as appears in Figs. 4a and 3c.

B. Fixed Temperature Gradients (Tilted 45 Deg)

Figure 5 shows the flow pattern and the solid–liquid interface morphology after the test cell is tilted 45 deg counterclockwise. Here, the cold wall is the tilted vertical wall on top, and the hot wall is below. The thermal gradients were varied the same as before. The flow patterns remain largely the same, that is, a single large loop recirculating the entire liquid pool. Similar to the series of cases when temperature gradients are perpendicular to the gravity, the velocities in the tilted cavity also decrease with a reduction of temperature gradients. Numerical model results are once again in good agreement with experimental measurements for both the flowfield and interface morphology. Both the numerical and the experimental results show that the tilted orientation of the cavity has relatively little effect on the interface shapes as compared to the vertical ones. The convection, as shown in Fig. 4a and Fig. 5a, however, is marginally stronger at the same wall temperature gradient for the tilted case, although the flow pattern is essentially the same. This occurrence seems perplexing because the tilted case has a smaller gravity component perpendicular to the thermal gradient (or a smaller driving force) and hence should have had a reduced flow. To resolve this puzzle, simulations were conducted for the same configuration but with hot and cold walls exchanged. A reduced flow was again indeed obtained. Further calculations with Fig. 5 for the same thermal gradients but no solidification also yield consistent results with a slightly increased flow. Detailed analyses attribute this phenomenon to the fact that, for this system, the gravity component parallel to the thermal gradient also contributes to the fluid's motion. For the configuration shown in Fig. 5, the Rayleigh number based on the gravity component parallel to the temperature gradient is much larger than the threshold (or critical) Rayleigh number and thus induces additional convective flows.[24] Thus, for this case the flow is driven by a combined force resulting from both perpendicular and parallel components, with the latter originated from the well-known Rayleigh–Benard convection.

C. Inverted Temperature Gradient

To clarify the effect of the Rayleigh–Benard convection on solidification, experiments and simulations were conducted for the configuration where the cell is tilted 90 deg with the hot wall at the bottom and the cold wall on the top. The other two walls are kept adiabatic. With data in Table 1, it is easily shown that the Rayleigh's instability condition is met for this condition and thermal convection starts to occur (Fig. 6). For these conditions, flow patterns are completely different from the preceding case and have a significant effect on the interface morphologies. The inverted temperature gradients, imposed in parallel walls but opposite to the gravity, result in two-loop flow and four-loop flow patterns, depending on the distance between the hot wall and the solidification interface. All of these loops share a common feature. That is, the flow moves downward along two sidewalls and moves upward somewhere inside the cavity depending on the imposed thermal gradients. This phenomenon is attributed to the boundary imperfections that are neglected in the classical theory of Rayleigh–Benard convection, which was discussed by Roppo et al.[25] As a result of the fluid layer being assumed to be infinitely long, the classical Rayleigh–Benard solution is degenerate in that it predicts the cellular convection structures of the flow but not flow directions, the latter having to rely on other information in the system.[25] In the present case, a very thin slit was cut on insulation on two sidewalls to allow the laser sheet to pass through and to illuminate the fluid, and there an imperfection of insulation is expected. Although this imperfect insulation did not cause a difference in predicted results for other cases just described, which were checked through numerical simulations, it determines the flow motion direction for the present case when the inverted thermal gradients are applied. Because of this imperfection, the fluid near the vertical wall is slightly cooler than the inside fluid. Hence, the liquid flows down along the vertical boundaries instead

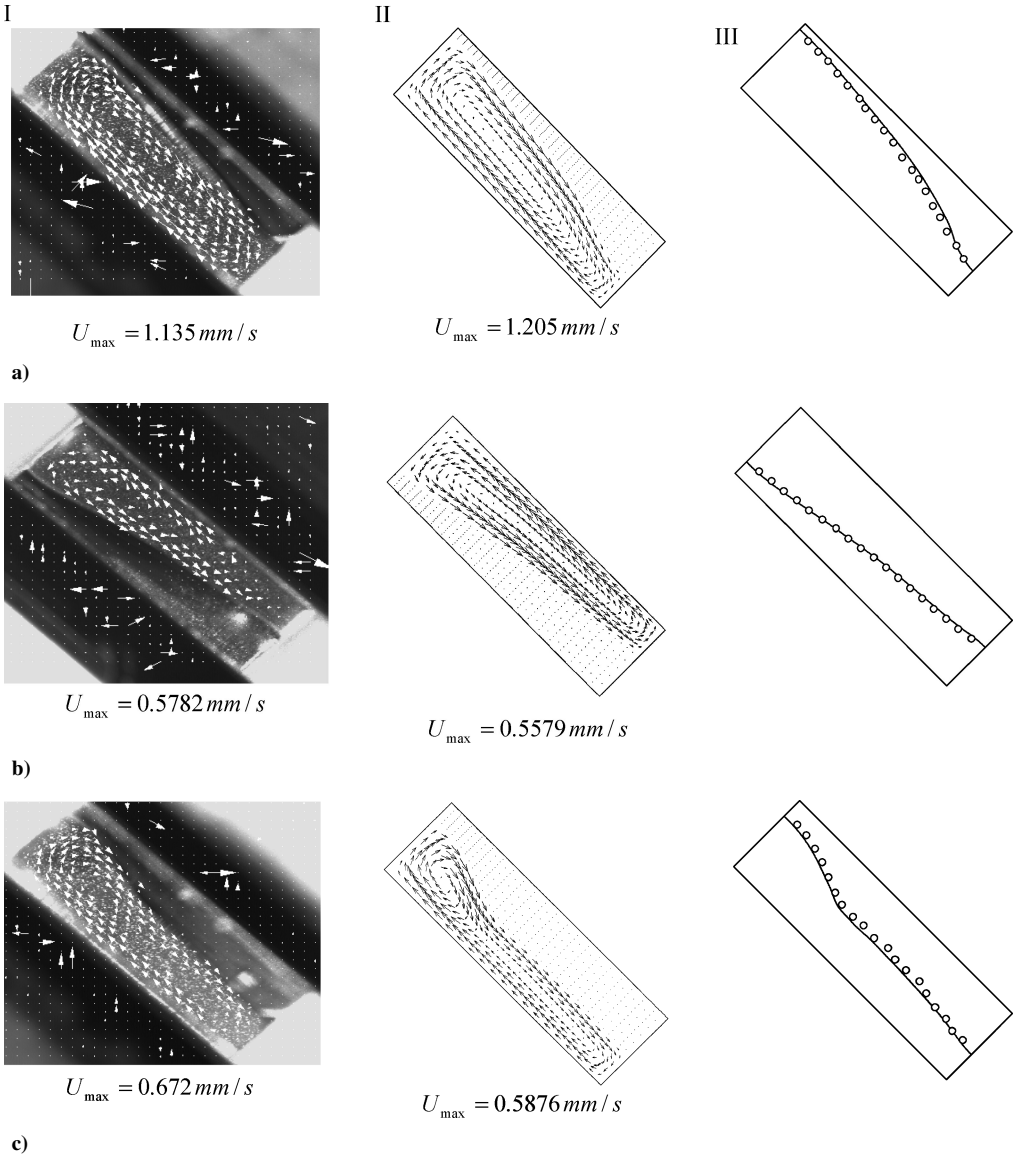

Fig. 5 Solidification of SCN under fixed temperature gradients within a tilted 45-deg cell. Plot region: 6.2 × 20 mm: a) T_L = 336.15 K, T_R = 328.65 K; b) T_L = 334.65 K, T_L = 328.65 K; and c) T_L = 333.65 K, T_R = 328.65 K.

of going up as it would if only vertical temperature gradients were applied.

To account for the boundary imperfections just discussed, the radiation boundary condition with an emissivity of 0.1 was applied at the two vertical walls. The computed results are given along with the experimental measurements for two different thermal gradient conditions. Clearly, agreement between the numerical and experimental results is obtained. Both experiments and simulations show that at the high thermal gradient the aspect ratio of the liquid pool is reduced (height over length), causing the flow structure to change from a two-loop pattern to a four-loop pattern.

For these cases, convection produces a conspicuous effect on the solidification interface morphology. When a two-loop convection recirculates in the liquid, the interface exhibits a single concave structure towards the liquid pool. The fluid stream gains its momentum from contacting the hot wall once it comes down along the vertical walls. It moves towards the middle and forms a hot jet rising upward towards the center. At the solid–liquid interface, it splits approximately equally and then moves towards the vertical walls. On the way, the hot fluid loses heat and becomes cooler. In the other case where a larger thermal gradient is imposed, the liquid pool is squeezed vertically, and the distance between the solidification front and the hot wall reduces approximately by a half. Here the flowfield displays a four-loop recirculating structure with two hot fluid streams arising from the bottom at approximately equal distances away from the vertical walls, with each producing a solid–liquid interface shape similar to the two-flow structure. The flow at the middle is down. These phenomena are well predicted by the numerical model and are verified by the experimental measurements.

D. Oscillating Temperature Gradients

With the finite element code validated by the experimental measurements, the numerical study was carried out on the solidification of SCN subject to oscillating temperature gradients. The fixed-grid method was used in this configuration to predict the flow pattern and interface shape and position because of the highly distorted solidification interface. For this configuration, the bottom wall is kept at a temperature (315 K) lower than melting point to induce solidification. The right wall is at a fixed temperature (332.19 K) 1 deg higher than the melting pointing, and the left wall is at an oscillating temperature whose average is the same as the right wall temperature. The frequency of the temperature oscillation is 0.005 Hz. A test cavity of the same dimension as previous experiments is used for this case (see Fig. 1b). The boundary temperatures for the computations are experimentally measured.[24]

As shown in Fig. 7, the numerical model accurately predicts the basic trend of flow rotation and interface shape changes with time

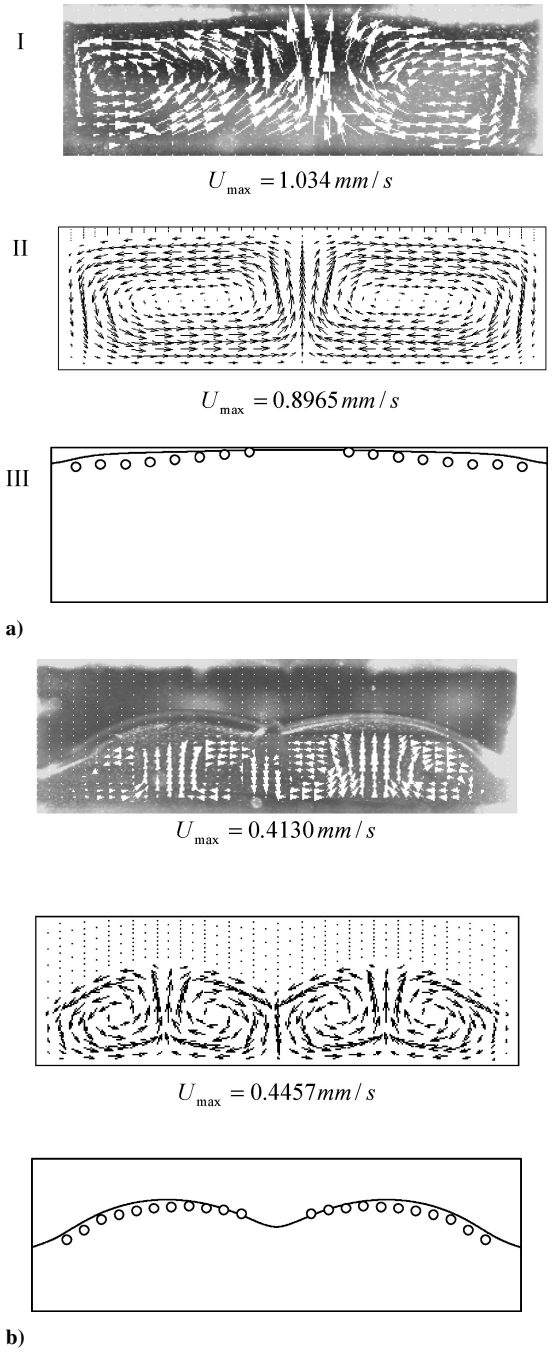

Fig. 6 Solidification of SCN under fixed temperature gradients in an inverted cavity. Plot region: 20 × 6.2 mm: a) $T_T = 330.95$ K, $T_B = 334.5$ K and b) $T_T = 328.85$ K, $T_B = 333.56$ K.

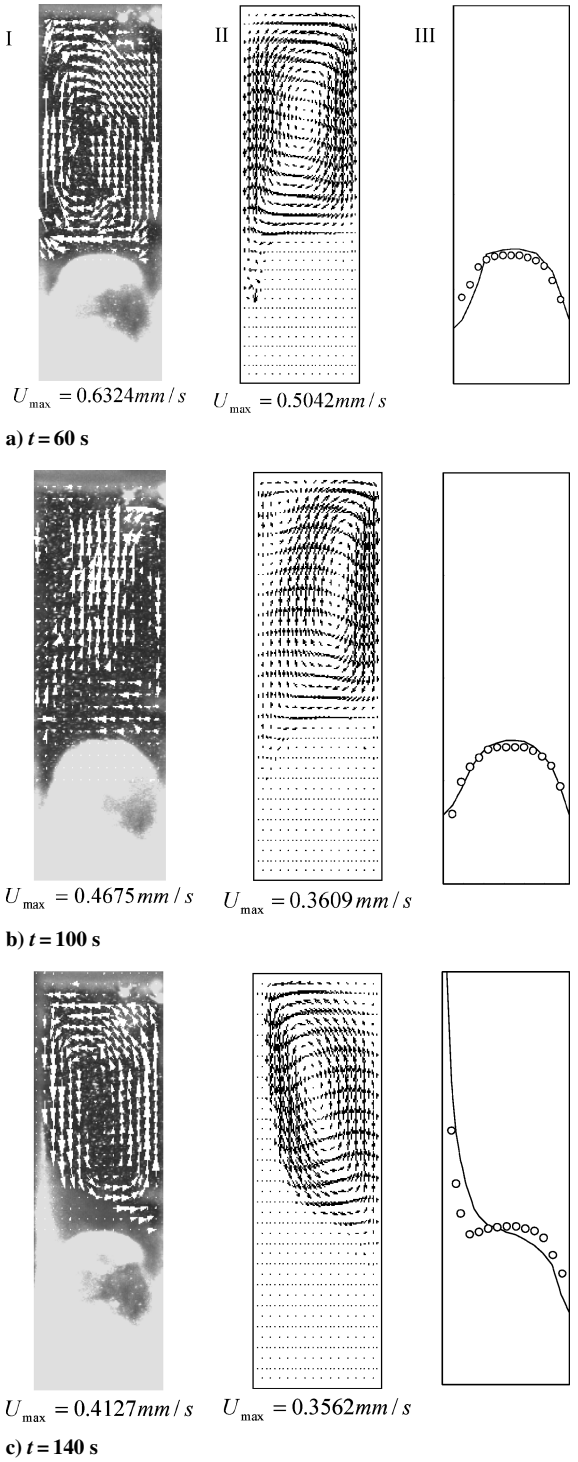

Fig. 7 Measurement and predictions of flow pattern and solid–liquid interface in oscillating temperature gradients: $F = 0.005$ Hz, $T_L = 332.19 + 2.0\sin(0.0314t)$ K, $T_R = 332.19$ K, and $T_B = 315$ K. Plot region 6.2 × 20.0 mm.

as affected by flow, which are verified by the experimental measurements. Although not as good as those the predications for the constant thermal gradient cases, this comparison is considered reasonably good, in light of the difficulties associated with performing this type of time-varying experiment. Detailed analysis of the experimental and numerical results reveals that the flow rotation follows approximately the same frequency cycle as boundary temperature oscillation, which is consistent with Stelian et al.[17] for other similar systems. At time $t = 60$ s, which is measured from a quasi-steady periodic cycle (same as what follows), the temperature of the left wall is higher than that of the right wall, and both walls have temperatures higher than T_m. One large convection loop goes up from the left wall and rolls down along the right wall as a result of the temperature gradient along the x direction. The solidification is primarily controlled by the vertical temperature gradient, which results in a block of solid matter that accumulates at the cold bottom wall.

At time $t = 100$ s, the temperatures of the two sidewalls are about equal, but the right wall temperature starts to ramp down. At this instant, a two-loop flow structure appears, moving down from the sidewalls and upward from inside of the liquid domain. Neglecting the oscillatory temperature gradient and the flow from the previous stage as an initial condition, the two vortices should be symmetric with equal strength and driven by the vertical temperature gradients. This is consistent with the results reported in Refs. 12 and 26. With the phase lag between the flow and the buoyancy driving force, the flow near the right wall still dominates the melt, but is weakened by a secondary flow at the top-left corner in the cavity

generated by the interaction of horizontal and vertical temperature gradients. At time $t = 140$ s, however, the temperature of the left wall is below T_m and also lower than the right wall temperature. Consequently, solidification occurs not only at the bottom, but also near the left sidewall. Temperature gradients in both the x and y directions play an important role in determining the solid–liquid interface. Hence, the interface morphology results from the contributions of both components, that is, the bottom solid comes from the vertical gradient, and the thin crust along the left sidewall comes from convection caused by the horizontal gradient. At this instant, the one-loop flow structure has returned, but it rotates in an opposite direction to that shown in the two instants (see Fig. 7a), manifesting the change in the direction of the thermal gradient. Further simulations indicate that the amplitude and frequency of the temperature oscillation have little effect on the convection pattern and interface morphology. Additional modeling studies on the amplitude and frequency effects on the melt flow and solidification phenomena in a system for microgravity applications have been reported in a recent publication.[21]

VII. Conclusions

In this paper, natural convection and solidification in a two-dimensional cavity driven by constant and oscillating temperature gradients have been studied experimentally and numerically. Numerical models based on the in-house finite element code were used to predict the flowfield, the temperature distribution, and the solid–liquid interface shape during solidification, with the wall temperatures input from experimental measurements. Both the fixed-grid and moving-grid methods were applied in the numerical simulations, with the former being used for the oscillating thermal gradient conditions and the latter being used for the constant temperature gradient conditions. A laser-based PIV system has been set up to visualize the flow patterns and interface shapes and to map out the convective velocity within the liquid pool during solidification. Under constant temperature gradients, one recirculating loop is developed in the melt, starting from the onset of solidification until a quasi steady state. The flow becomes weaker with a decrease in temperature gradients. This holds true for both the vertical configuration of the cavity, where the gravity is perpendicular to the thermal gradient, and the tilted configuration, where the gravity acts at an angle with the cavity. The convective flow has a very strong effect on the solid–liquid interface shape. The interface changes with the change of the fixed temperature gradients. But a change of the test cell angle relative to gravity has little effect on the flow pattern of the melt and hence solid–liquid front morphology. Numerical simulations and experimental measurements are in good agreement for flow pattern, velocity magnitude, and interface morphologies for constant thermal gradients. The comparison is also reasonably good for flow rotation and interface shape changes during solidification under oscillating thermal gradients.

Acknowledgments

Support of this work by NASA (Grant no. NAG8-1693) is gratefully acknowledged, and so is the assistance of R. Lentz with the experimental setup and instrumentation.

References

[1]Fleming, M. C., *Solidification Processing*, 1st ed., McGraw–Hill, New York, 1974, Chap. 1.

[2]Tiller, W. A., *The Science of Crystallization: Macroscopic Phenomena and Defect Generation*, 1st ed., Cambridge Univ. Press, New York, 1991, Chap. 1.

[3]Langlois, W. E., "Buoyancy-Driven Flows in Crystal-Growth Melts," *Annual Review of Fluid Mechanics*, Vol. 17, 1985, pp. 191–215.

[4]Glicksman, M. E., Coriell, S. R., and McFadden, G. B., "Interaction of Flows with the Crystal-Melt Interface," *Annual Review of Fluid Mechanics*, Vol. 18, 1986, pp. 307–335.

[5]Singh, V. K., and Prescott, P. J., "Convective Transport Phenomena During Solidification of a Binary Metal Alloy," *Proceeding of National Heat Transfer Conference*, American Society of Mechanical Engineers, Vol. 323, Fairfield, NJ, 1996, pp. 79–86.

[6]Shahani, H., Amberg G., and Fredriksson, H., "On the Formation of Macrosegregations in Unidirectionally Solidified Sn-Pb and Pb-Sn Alloy," *Metallurgical Transctions A*, Vol. 23A, No. 8, 1992, pp. 2301–2311.

[7]Prescott, P. J., and Incropera, F. P., "Numerical Simulation of a Solidifying Pb-Sn Alloy. The Effects of Cooling Rate on Thermosolutal Convection and Macrosegregation," *Metallurgical Transctions B*, Vol. 22, No. 4, 1991, pp. 529–540.

[8]Prabhakar, O., "Solidification Modeling," *Bulletin of Material Science*, Vol. 16, No. 6, 1993, pp. 543–560.

[9]Simpson, J. E., and Garimella, S. V., "Investigation of the Solutal, Thermal and Flow Fields in Unidirectional Alloy Solidification," *International Journal of Heat and Mass Transfer*, Vol. 41, No. 16, 1998, pp. 2485–2502.

[10]Yeoh, G. H., de Vahl Davis, G., Leonardi, E., de Groh, H. C., III, and Yao, M., "A Numerical and Experimental Study of Natural Convection and Interface Shape in Crystal Growth," *Journal of Crystal Growth*, Vol. 173, Nos. 3–4, 1997, pp. 492–502.

[11]Simpson, J. E., Garimella, S. V., and de Groh, H. C., III, "Experimental and Numerical Investigation of the Bridgman Growth of a Transparent Material," *Journal of Thermophysics and Heat Transfer*, Vol. 16, No. 3, 2002, pp. 324–335.

[12]Benielli, D., Ganaoui, M. E., Semma, E., Bergeon, N., Jamgotchian, H., Voge, P., Billia, B., and Bontoux, P., "Effect of Thermal Convection on Directional Solidification of Succinonitrile-Acetone Alloy: Comparison Between Experimenta and Numerical Studies," *Journal De Physique IV*, Vol. 11, No. 6, 2001, pp. 135–142.

[13]Cao, W. Z., and Poulikakos, D., "Solidification of an Alloy in a Cavity Cooled Through Its Top Surface," *International Journal of Heat and Mass Transfer*, Vol. 33, No. 3, 1990, pp. 427–434.

[14]Cao, W. Z., and Poulikakos, D., "Transient Solidification of a Binary Mixture in an Inclined Rectangular Cavity," *Journal of Thermophysics and Heat Transfer*, Vol. 6, No. 2, 1992, pp. 326–332.

[15]Giangi, M., Kowalewski, T. A., Stella, F., and Leonardi, E., "Natural Convection During Ice Formation, Numerical Simulation vs. Experimental Results," *Computer Assisted Mechanics and Engineering Science*, Vol. 7, No. 3, 2000, pp. 321–342.

[16]Davis, S. H., Müller, U., and Dietsche, C., "Pattern Selection in Single-Component Systems Coupling Bénard Convection and Solidification," *Journal of Fluid Mechanics*, Vol. 144, July 1984, pp. 133–151.

[17]Stelian, C., Duffar, T., Santailler, J. L., and Nicoara, I., "Influence of Temperature Oscillation on the Interface Velocity During Bridgman Crystal Growth," *Journal of Crystal Growth*, Vol. 237–239, No. 1–4, 2002, pp. 1701–1706.

[18]Pradeep, N., Kang, H. J., Lin, C. X., and Ebadian, M. A., "The Influence of Boundary Condition on Solidification of Binary Solution in Rectangular Cavity," *Proceedings of National Heat Transfer Conference*, American Society of Mechanical Engineers, Vol. 364-2, Fairfield, NJ, 1999, pp. 185–190.

[19]Skudarnov, P. V., Lin, C. X., Wang, M. H., Pradeep, N., and Ebadian, M. A., "Evolution of Convection Pattern During the Solidification of a Binary Mixture," *International Journal of Heat and Mass Transfer*, Vol. 45, No. 26, 2002, pp. 5191–5200.

[20]Shu, Y., Li, B. Q., and de Groh, H. C., III, "Numerical Study of g-Jitter Induced Double-Diffusive Convection," *Numerical Heat Transfer, A, Application*, Vol. 39, No. 3, 2001, pp. 245–265.

[21]Li, K., Li, B. Q., and deGroh, H. C., III, "Numerical Analysis of Double-Diffusive Convection/Solidification Under g-Jitter/Magnetic Fields," *Journal of Thermophysics and Heat Transfer*, Vol. 17, No. 2, 2003, pp. 199–209.

[22]Voller, V. R., Cross, M., and Markatos, N. C., "Enthalpy Method for Convection/Diffusion Phase Change," *International Journal for Numerical Methods in Engineering*, Vol. 24, No. 1, 1987, pp. 271–284.

[23]Goldstein, R. J., *Fluid Mechanics Measurements*, Taylor and Francis, Washington, DC, 1996, Chap. 4.

[24]Shu, Y., "An Experimental and Numerical Study of Natural Convection and Solidification in Constant and Oscillating Temperature Fields," Ph.D. Dissertation, Mechanical Engineering Dept., Washington State Univ., Pullman, Dec. 2003.

[25]Roppo, M. N., Davis, S. H., and Rosenbalt, S., "Bénard Convection with Time-Periodic Heating," *Physics of Fluids*, Vol. 27, No. 4, 1984, pp. 796–803.

[26]Ganaoui, M. E., Lamazouade, A., Bontoux, P., and Morvan, D., "Computational Solution for Fluid Flow Under Solid/Liquid Phase Change Conditions," *Computers and Fluids*, Vol. 31, Nos. 4–7, 2002, pp. 539–556.